

3d Transition Metal Intercalation into Layered TiS_2 Crystal

Hiroshi NEGISHI

Reprinted from

JOURNAL OF SCIENCE OF THE HIROSHIMA UNIVERSITY
Series A, Vol. 51, No. 2, AUGUST 1987

3d Transition Metal Intercalation into Layered TiS_2 Crystal

Hiroshi NEGISHI

Department of Materials Science, Faculty of Science,
Hiroshima University, Higashisenda-machi, Naka-ku, Hiroshima 730

(Received: May 20, 1987)

Systematic studies on the structural and magnetic properties of 3d transition metal intercalation compounds of M_xTiS_2 ($\text{M} = \text{V}, \text{Cr}, \text{Mn}, \text{Fe}, \text{Co}, \text{and Ni}$; $0 \leq x \leq 1$) have been carried out by X-ray powder diffraction, low-field ac magnetic susceptibility, magnetization, and ^{57}Fe Mössbauer spectroscopy measurements. The interlayer spacing c depends remarkably on the 3d metals and their concentrations, while the intralayer spacing a is less dependent on these quantities. Such a behavior can be explained semiempirically by a model based on the concept of "resonance" in chemical bonding. Various types of magnetic phases in M_xTiS_2 have been found and their magnetic properties can be understood in terms of an itinerant or band picture rather than a localized or rigid band model, in agreement with the recent band calculations using a self-consistent APW method.

1. Introduction

Transition metal dichalcogenides TX_2 ($\text{T} = \text{IV}, \text{V}, \text{VI}$ groups; $\text{X} = \text{S}, \text{Se}, \text{Te}$) with layered structures have been of current interest because their structural and electronic properties are of low-dimensional character.¹⁾ They consist of a hexagonal layer of transition metal T atoms sandwiched by two similar layers of chalcogen X atoms, where the basic X-T-X layers are coupled by weak van der Waals forces. According to the types of stacking of these basic layers, there are several polytypes (1T, 2H, 3R, etc.). In these compounds various guest atoms, such as alkali metals²⁾ and 3d transition metals,³⁻⁵⁾ enter into van der Waals gaps of TX_2 layers, usually accompanying the change in lattice spacings a and c , and the formation of a superstructure at particular guest concentrations. In particular, the interlayer spacing c is varied appreciably with the guest concentration x , as found in Li_xTiS_2 ⁶⁾ and M_xZrS_2 ($\text{M} = \text{Fe}, \text{Co}, \text{and Ni}$).⁷⁾ Furthermore, various types of magnetism have been reported in 3d transition metal intercalates M_xTX_2 ($\text{M} = \text{Ti}, \text{V}, \text{Cr}, \text{Mn}, \text{Fe}, \text{Co}, \text{and Ni}$). In group V dichalcogenides of NbS_2 , TaS_2 , and NbSe_2 , for examples, there have been found para-, ferro-, antiferro-, and metamagnetism depending on the kind of 3d metals and their concentrations.^{3-5,8)} Their magnetic properties have been understood in terms of a localized electron or rigid band model.⁸⁻¹²⁾ In these group V dichalcogenides, the guest 3d metals usually occupy

the octahedral holes and contribute part of the electrons to the already half-filled host d_{z^2} band. The intercalated 3d metals are in divalent or trivalent ion states and subject to a strong crystalline field. Similar studies have been made on one of the group IV dichalcogenides, TiS_2 , an n-type degenerate semiconductor having a simple 1T-CdI_2 type structure; paramagnetism in V_xTiS_2 ¹³⁾ and Ni_xTiS_2 ,¹⁴⁾ spin-glass and ferromagnetism in Fe_xTiS_2 ,^{14,15)} and antiferromagnetism in $\text{Fe}_{1/2}\text{TiS}_2$ ¹⁶⁾ and Co_xTiS_2 ¹⁴⁾. Some 3d transition metals are known to occupy the octahedral holes in the TiS_2 layers, and gradually fill up the available holes which leads to the rhombohedral defect NiAs type structure.^{3,4)} Recently, photoemission studies on the Fe and Ni intercalates have revealed that the guest atom 3d orbitals hybridize with the host Ti 3d and S 3p orbitals.¹⁷⁾ Furthermore, the energy band calculations of M_xTiS_2 ($\text{M} = \text{Cr}$ and Fe) have been made using a self-consistent APW method, predicting the itinerant character of magnetism in M_xTiS_2 .^{18,19)}

In the present work comprehensive studies on the structural and magnetic properties of M_xTiS_2 ($0 \leq x \leq 1$) have been performed to understand the intercalation phenomena in these layered compounds. Here TiS_2 has been chosen as a host material because it is stable in air and moisture and has the simple 1T-CdI_2 type structure compared with other materials having various polytypes. The X-ray powder diffraction shows that the lattice spacings a and c of M_xTiS_2 depend on the 3d metals and their concentrations. The remarkable change in the interlayer spacing c can be understood, based on the concept of "resonance" in chemical bonding introduced by Pauling,²⁰⁾ using a semiempirical model which takes into account the ionic radii, interatomic distance, force constants, bond covalency, as well as the formation of a superstructure. Furthermore, in order to clarify the magnetic properties of M_xTiS_2 , low-field ac magnetic susceptibility (1.5-300 K), magnetization in static and pulsed fields (4.2, 77, 300 K), and ^{57}Fe Mössbauer spectroscopy (300 K) have been measured. These experimental data show that M_xTiS_2 have itinerant magnetic character, in good agreement with the theoretical predictions.^{18,19)} In what follows, we shall describe the details of experimental procedure, results and discussion, and summary.

2. Experimental

The 3d transition metal intercalates M_xTiS_2 were grown by a chemical vapor transport technique in a single-zone furnace with a small temperature gradient. The starting elements all in powder form and iodine of 5-15 mg/cm^3 as a carrier gas were charged at a required ratio in an evacuated quartz ampoule (10-20 mm bore diameter and 100-150 mm long); the purity was 99.5% for V, 99.9% for Ti, and 99.99% for other elements (S, Cr, Mn, Fe, Co, and Ni). The ampoule was placed in a home-made single-zone furnace for 3 days-1 week at 800-900 °C, with a temperature difference $\Delta T = 20\text{-}30$ °C at both ends of the ampoule. Precautions at a heating stage were taken to stabilize the chemical reaction; in particular, the holding at 500 °C for at least half a day was desired to avoid an explosion. Typically, V and Cr intercalates were small crystallites with thickness of 0.01-0.05 mm (roughly $1 \times 1 \text{ mm}^2$ for $x < 1/2$ and less than $0.2 \times 0.2 \text{ mm}^2$ for $x > 1/2$), while those of Mn, Fe,

Co, and Ni were grown in the form of thin flakes up to $8 \times 8 \text{ mm}^2$ with thickness 0.05-1 mm; for $x > 1/2$ it was usually difficult to grow flakes as large as $5 \times 5 \text{ mm}^2$. Mn intercalation was available only up to $x = 1/3$, beyond which a metal sulfide like MnS was produced because the chemical affinity between Mn and S is strong. All the grown crystals were shown by X-ray powder diffraction to have a 1T-CdI_2 type structure over the whole composition range $0 \leq x \leq 1$. The electron diffraction patterns for the Mn, Fe, Co, and Ni intercalates revealed the $2a \times 2a$ and $\sqrt{3}a \times \sqrt{3}a$ superstructure solely at the characteristic concentrations $x = 1/4$ and $1/3$, respectively, as found by many workers.^{3,4)} For magnetic measurements the crystals were ground into fine powders, which were then pressed into a cylindrical form (nearly 3 mm in diameter and 4 mm long). In particular, for anisotropy studies, the single crystalline flakes were glued to each other with a vanish into a rectangular form.

The ac magnetic susceptibility measurements (80 or 200 Hz, 3 Oe)²¹⁾ were performed by a mutual inductance bridge over the temperature range 1.5-300 K. The ac susceptibilities in static fields up to 5 kOe produced by a superconducting magnet were also measured.

Magnetization measurements under static fields up to 20 kOe were performed by a home-made vibrating sample magnetometer (VSM). In order to get high sensitivity, a pair of sample pick-up coils (copper wires of 0.05 mm in diameter) were set in an inner He glass dewar with its coil axis parallel to an applied field. Static fields up to 20 kOe were supplied from an electromagnet (Tamagawa Co., TM-WF10618R-200). A sample holder was oscillated at frequency of 70 Hz by an electromechanic vibrator (IMV Lab. Cor., PET-01), which was driven by a reference voltage from a lock-in-amplifier (NF, LIA-572B). The output signal of the sample pick-up coils was detected by the lock-in-amplifier, whose signal and an output of a magnetometer (Yokogawa, 3251) were traced by an X-Y recorder (Watanabe, WX4421) to obtain magnetization curves. High field magnetizations up to 160 kOe were measured using a home-made small-sized pulse magnet. The pulse magnet itself is a solenoidal coil of copper wires (1.5 mm in diameter) wound around a fiber-glass reinforced plastics (FRP) bobbin; its inner and outer diameters, and length are 25, 43, and 67 mm, respectively. A pulsed field was switched on by a silicon thyristor through electrolytic condensers (charge capacity of 11 kJ at 800 V), a pulse duration being about 30 ms. The absolute values of magnetization for both experimental setups were calibrated with respect to those of pure nickel metal and paramagnetic Gd_2O_3 powder. The static and pulsed magnetizations were measured at fixed temperatures of 4.2, 77 and 300 K.

The ^{57}Fe Mössbauer spectra for Fe_xTiS_2 were measured at 300 K using a $^{57}\text{Co}/\text{Rh}$ source. The observed spectra were analyzed by a least-square method. The velocity scale was calibrated with the six lines of an α -Fe metallic foil, so that the isomer shifts were taken with reference to α -Fe.

3. Results and discussion

3. 1. Structural properties

Figure 1 shows the observed lattice spacings a and c of M_xTiS_2 plotted against

the metal concentration for different guest atoms. Upon intercalation of 3d metals the intralayer spacing a remains almost unchanged while the interlayer spacing c varies appreciably with the 3d metals and their concentrations. Similar variations have been found for $M_x\text{ZrS}_2$ ($M = \text{Fe}, \text{Co}, \text{and Ni}$),⁷⁾ in which the M atom occupies the tetrahedral holes of ZrS_2 layers. Figure 2 depicts the value c at $x=1$ as a function of the atomic number of M ; for Mn the extrapolated value at $x=1$ from Fig. 1 is used. As found in $M_{1/2}\text{NbS}_2$,²²⁾ where the M atom is at octahedral sites, such a plot is in good agreement with a similar plot of ionic radii $r^i(M^{2+})$ of the divalent metal ions M^{2+} , where the values of $r^i(M^{2+})$ are denoted by solid circles for a low-spin state and by open circles for a high-spin state, with the coordinate number 6 (see Table I).²³⁾ Though the 3d metal ions in TX_2 layers are reported to be divalent or trivalent, Fig. 2 indicates that the valence state of the M atom is divalent with a high-spin state; only the Co ion is considered to be a low-spin state ($d\epsilon)(d\gamma)^1$, in good agreement with the ESR data.²⁴⁾

In what follows, we shall give a semiempirical explanation for the variation of the interlayer spacing c with intercalation of 3d transition metals into TiS_2 layers on the basis of the concept of "resonance" in chemical bonding. The change in the intralayer spacing a is negligibly small, which hereafter we take as a constant. As shown in Fig. 1, the value of c is not a monotonic function of x , but in some cases it attains a minimum or maximum at $x = 1/4$ – $1/2$, where the formation of a superstructure or atomic ordering is found by the electron diffraction. In the following we shall first neglect such an atomic ordering and later take it into consideration.

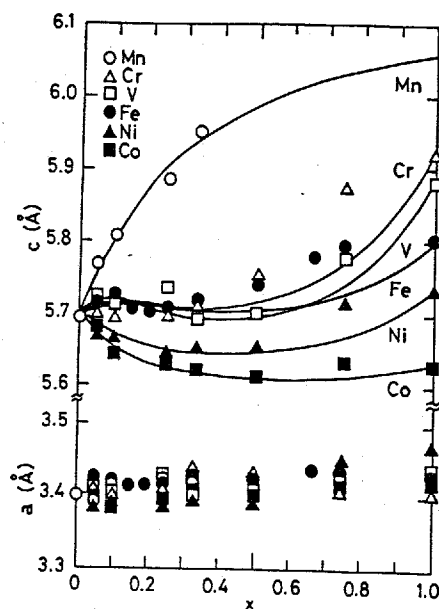


Fig. 1. Observed lattice spacings a and c plotted against the nominal 3d transition metal concentration x for 1T- CdI_2 type $M_x\text{TiS}_2$ ($M = \text{V}, \text{Cr}, \text{Mn}, \text{Fe}, \text{Co}, \text{and Ni}$). The solid curves are the calculated interlayer spacing $c(x)$ for $M_x\text{TiS}_2$ obtained by using eqs. (1), (2), and (6), with the best fit values of Table II.

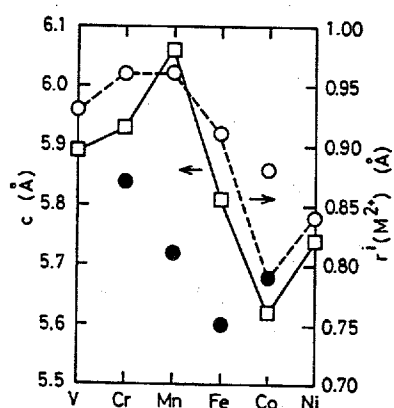


Fig. 2. Variation of the interlayer spacing c as a function of the atomic number of M for MTiS_2 . The ionic radii $r^i(M^{2+})$ for each divalent ion M^{2+} with coordination number 6 are also shown; open circles denote a high-spin state and solid circles a low-spin state.²³⁾

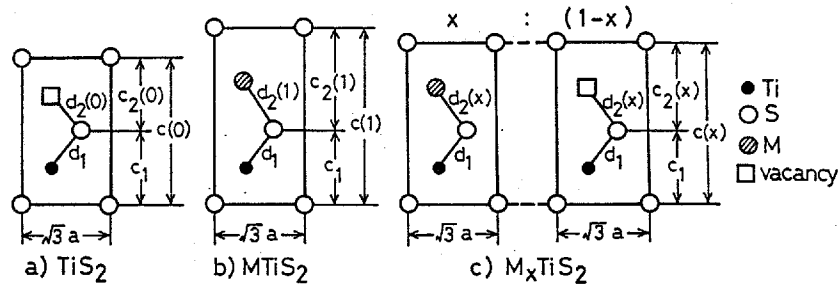


Fig. 3. $(11\bar{2}0)$ sections of (a) TiS_2 ($x = 0$), (b) MTiS_2 ($x = 1$), and (c) M_xTiS_2 ($0 < x < 1$). A square in (a) is a vacant site in the van der Waals gap with octahedral symmetry, into which the guest atom M intercalates (see text for other notations).

A. Resonance model

Figure 3 shows schematically the $(11\bar{2}0)$ planes of (a) 1T-CdI₂-type TiS_2 ($x = 0$), (b) a completely intercalated state of MTiS_2 ($x = 1$), and (c) a partially intercalated state of M_xTiS_2 ($0 < x < 1$) which we regard as a "resonant state" between the TiS_2 and MTiS_2 states at a ratio of $(1 - x) : x$. In TiS_2 the octahedral position in the van der Waals gap is vacant, denoted by a square, while in MTiS_2 the guest atom M occupies this position. Furthermore, we assume the interlayer spacing c to be the sum of two sublayer spacings, as shown in Fig. 3. Thus the interlayer spacing of TiS_2 , denoted here by $c(0)$, is given by the sum of c_1 and $c_2(0)$, where c_1 is the spacing of a S-Ti-S sublayer and $c_2(0)$ that of a S-vacancy-S sublayer (van der Waals gap). Similarly the interlayer spacing of MTiS_2 , denoted by $c(1)$, is given by the sum of c_1 and $c_2(1)$, where $c_2(1)$ is the spacing of a S-M-S sublayer. Also we take into account the interatomic distances or bond lengths d_1 between the S and Ti atoms and $d_2(0)$ between the vacancy and S atom for TiS_2 ; similarly d_1 and $d_2(1)$ for M_xTiS_2 as shown. Hereafter we assume that c_1 , d_1 , and the intralayer spacing a are all constant. Then for a partially intercalated compound M_xTiS_2 , the interlayer spacing $c(x)$ can be expressed by

$$c(x) = c_1 + c_2(x), \quad (1)$$

where from a simple geometrical relation c_1 and $c_2(x)$ are given as

$$c_1 = 2(d_1^2 - a^2/3)^{1/2}, \quad c_2(x) = 2[d_2(x)^2 - a^2/3]^{1/2}, \quad (2)$$

respectively. Here $d_2(x)$ is the bond length between the S atom and M atom or vacancy. In this model we assume that only $d_2(x)$ is dependent on x and the M_xTiS_2 state is the resonant state between the TiS_2 and MTiS_2 at the ratio $(1 - x) : x$, as mentioned above.

Now the lattice constants of TiS_2 are found to be $a = 3.41 \text{ \AA}$ and $c = 5.70 \text{ \AA}$, and the positions of the S atoms are $(0, 0, 0)$ and $(2a/3, 2a/3, c/2)$. Thus d_1 and $d_2(0)$ for $x = 0$ are calculated to be $d_1 = d_2(0) = 2.43 \text{ \AA}$ from eqs. (1) and (2).

Table I. Interlayer spacing $c(1)$, interatomic distance $d_2(1)$, ionic radii $r^i(M^{2+})$ of divalent metal ion M^{2+} , and ionic bond distance $d_2^i(M^{2+})$ defined by eq. (3) (In units of Å)

	V	Cr	Mn	Fe	Co	Ni
$c(1)$	5.89	5.93	6.06 ^a	5.81	5.62	5.74
$d_2(1)$	2.49	2.50	2.54	2.46	2.41	2.44
$r^i(M^{2+})^b$	0.93	0.96	0.96	0.91	0.79 ^c	0.84
$d_2^i(M^{2+})$	2.63	2.66	2.66	2.61	2.49	2.54

Other parameters used: $a = 3.41$, $c = 5.70$, and $r^i(S^{2-}) = 1.70$

^aExtrapolated value from Fig. 1

^bReference 22)

^cValue at a low-spin state

These values are given in Table I, where the ionic radii $r^i(M^{2+})$ of each divalent cation M^{2+} with the coordination number 6 at a high-spin state (Co^{2+} : low-spin state)²³⁾ and the ionic bond distances $d_2^i(M^{2+})$ for M^{2+} ion defined as

$$d_2^i(M^{2+}) = r^i(M^{2+}) + r^i(S^{2-}) \quad (3)$$

are also shown. Here $r^i(S^{2-})$ is the ionic radius of a S^{2-} ion ($= 1.70$ Å). As shown in Fig. 4, it is apparent that there is a strong correlation between the interatomic distance $d_2(1)$ and ionic bond distance $d_2^i(M^{2+})$ compared with the lattice constant c vs. ionic radii $r^i(M^{2+})$ relation shown in Fig. 2. However, $d_2(1)$ is not exactly equal to $d_2^i(M^{2+})$, but $d_2(1) < d_2^i(M^{2+})$ always, indicating that the M-S bond is not completely ionic but partially covalent.

Then the interatomic distance $d_2(x)$ for M_xTiS_2 ($0 < x < 1$) can be estimated. By analogy with the potential function for resonant bonding between a single bond and double bond for carbon-carbon bonds such as in benzene,²⁰⁾ we express the potential function for the M-S bond as the sum of two parabolic functions, representing the vacancy-S bond and the M-S bond potential functions, with coefficients $(1 - x)$ and x , respectively:

$$V(d_2(x)) = (1 - x)k_2(0)[d_2(x) - d_2(0)]^2/2 + xk_2(1)[d_2(x) - d_2(1)]^2/2, \quad (4)$$

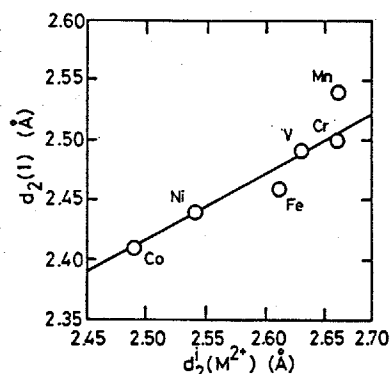


Fig. 4. The interatomic distance $d_2(1)$ between the M and S atoms for a completely intercalated compound $MTiS_2$ plotted against the ionic bond distance $d_2^i(M^{2+}) = r^i(M^{2+}) + r^i(S^{2-})$.

where the metal concentration x is used instead of the bond number n employed by Pauling. $k_2(0)$ and $k_2(1)$ are the force constants for the vacancy-S and M-S bonds, respectively. The equilibrium value of $d_2(x)$ can be found by setting the derivative of eq. (4) with respect to $d_2(x)$ equal to zero. Thus we have

$$d_2(x) = [1 + (\alpha\beta - 1)x]d_2(0)/[1 + (\alpha - 1)x], \quad (5)$$

where $\alpha = k_2(1)/k_2(0)$ is the ratio of the force constants and $\beta = d_2(1)/d_2(0)$ that of the bond lengths for the M-S and vacancy-S bonds. The equilibrium interatomic distance $d_2(x)$ is therefore a hyperbolic function of x and it can be specified by the two ratios α and β . The schematic forms of $d_2(x)$ are plotted in Fig. 5 for various cases. We see that $d_2(x)$ is an increasing function for $\beta > 1$, decreasing for $\beta < 1$, or constant for $\beta = 1$.

Furthermore, the ratio α specifies the form of the curve, whether it is convex, concave, or linear. In M_xTiS_2 the force constant $k_2(1)$ for the M-S bond is considered to be larger than $k_2(0)$ for the vacancy-S bond ($\alpha > 1$), and the variation of $d_2(x)$ is expected to be that of curves 1 or 7 in Fig. 5. Similar curves for the interlayer spacing $c(x)$ are readily obtained from eqs. (1), (2), and (5). However, these calculated curves do not simulate the observed results (except for Mn intercalates) shown in Fig. 1 having a maximum or minimum at $x = 1/4-1/2$.

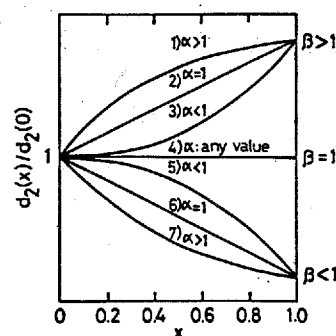


Fig. 5. Schematic drawing of $d_2(x)$ as a function of x for different values of α and β .

B. Modification of the resonance model

The foregoing simplified model has shown that $d_2(x)$ is a monotonically increasing or decreasing function of x , independent of the distribution of guest atoms. In actual case, a superstructure is formed at particular concentrations ($x = 1/4-1/2$), where the interlayer spacing c attains a maximum or a minimum. In order to take account of such an atomic ordering in the calculation of $d_2(x)$, we have attempted to add an extra entropic term to eq. (5),

$$d_2(x) = [1 + (\alpha\beta - 1)x]d_2(0)/[1 + (\alpha - 1)x] + \gamma [x \ln x + (1 - x) \ln(1 - x)], \quad (6)$$

where γ is an adjustable parameter denoting the degree of lattice contraction caused by a bond covalency due to the atomic ordering. Using eqs. (1), (2), and (6), we have calculated the values $c(x)$ as a function of x for each guest atom, and the results are shown in Fig. 1. The best fit values of α and γ used are listed in Table II; the parameter $\beta = d_2(1)/d_2(0)$ is evaluated from Table I.

The calculated and observed curves are in qualitative agreement; the fitting is good for V, Mn, Co, and Ni, while it is poor for Fe and Cr. Furthermore, in the

Table II. Best fit values $\alpha = k_2(1)/k_2(0)$ and γ in eq. (6) used in the calculation of Fig. 1

	V	Cr	Mn	Fe	Co	Ni
α	10	10	4	10	10	1
γ (Å)	0.08	0.08	0.0	0.035	0.01	0.01

range $1/2 < x < 1$ the calculated values are a little smaller than the observed values; in this range atomic ordering may be neglected. From the present model calculation the following features are noted. The ratio of the force constants $\alpha = k_2(1)/k_2(0)$ is of the order of 10 (except for Ni atom), which means that upon intercalation with 3d transition metals a much stronger bonding between the sublayers than the original van der Waals bonding is induced, making their character more three-dimensional; in other words, the intercalation compounds M_xTiS_2 lose their two-dimensional character and they are no longer layer compounds, as described by Vandenberg-Voorhoeve.³⁾ In addition, except for Mn intercalates ($\gamma = 0$), we note that the values of γ for V and Cr intercalates, whose M-S bond ionicity is high,²⁰⁾ are large compared with those of Fe, Co, and Ni intercalates whose M-S bond ionicity is low, which in turn suggests that the atomic ordering is more effective for the M-S bonds of higher ionicity than for those of lower ionicity (or more covalent M-S bond), leading to a lattice contraction.

3.2. Magnetic properties

3.2.1. V_xTiS_2

V_xTiS_2 shows a paramagnetic Curie-Weiss behavior, whose ac susceptibility χ is expressed in the form $\chi = \chi_0 + C/(T - \Theta)$, where χ_0 is a background term, C a Curie constant, Θ a paramagnetic Curie temperature. The magnetization curves at 4.2, 77, and 300 K for V_xTiS_2 ($0 \leq x \leq 1$) are linear to an applied field H , indicating paramagnetism, in good agreement with the ac magnetic susceptibility data. These results agree with those by other workers for V_xTiS_2 ($x \leq 1/3$).¹³⁾ On the other hand, ferromagnetic orderings have been found in $V_{1/3}NbS_2$ and $V_{1/3}TaS_2$ by Parkin et al.,¹²⁾ whereas Hulliger et al. have reported no magnetic orderings down to 2 K.⁹⁾

3.2.2. Cr_xTiS_2

Figure 6 shows the results for Cr_xTiS_2 . The ac susceptibility χ for $x = 0.05$ follows the Curie-Weiss law over the temperature range covered, and those for $0.10 \leq x \leq 1/3$ tend to level off at low temperatures. For $x > 1/3$, the χ - T curves look like some antiferromagnetic or perhaps spin-glass behavior. $Cr_{1/2}TiS_2$ shows two breaks in the curve at 15 and 30 K, where it is possible that the magnetic spins become slightly misaligned. Typical magnetization curves at 4.2 K for

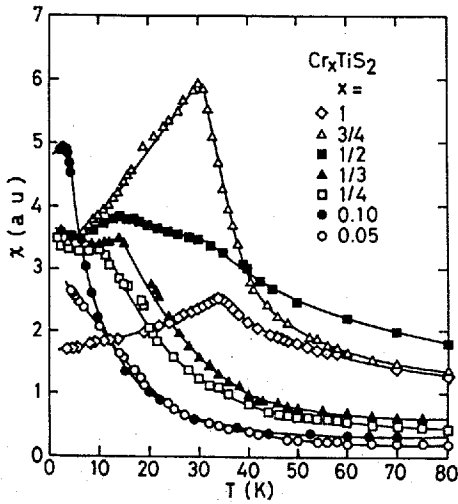


Fig. 6. Temperature dependence of the ac magnetic susceptibility of Cr_xTiS_2 .

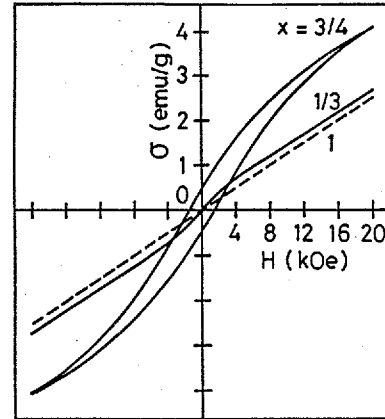


Fig. 7. Magnetization curves at 4.2 K for Cr_xTiS_2 .

Cr_xTiS_2 with $x = 1/3$, $3/4$, and 1 are shown in Fig. 7. The σ - H curve for $x = 1/3$ is nearly linear and that for $x = 1$ is linear, while the sample with $x = 3/4$ shows a clear hysteresis curve with a coercive force $H_c \sim 1.5$ kOe. Considering these ac susceptibility and magnetization data, we may conclude that the magnetic phase is ferromagnetic over the whole Cr composition range except for $x = 1$, as shown in Fig. 8. Only CrTiS_2 ($x = 1$) is considered to be antiferromagnetic because of the presence of a cusp in the χ - T curve.

3.2.3. Mn_xTiS_2

Typical paramagnetic behaviors for Mn_xTiS_2 ($x \leq 1/3$) are shown in Fig. 9. The ac susceptibilities increase with Mn concentration up to $x = 0.10$, while they decrease for $x \geq 1/4$. The intensities of ac susceptibilities χ or initial susceptibilities at 4.2 K show three distinct Mn concentration regions, as shown in Fig. 10; the intensity χ increases with x up to 0.03 and becomes constant for $0.03 \leq x \leq 0.10$, followed by a decrease. Figure 11 shows the results of magnetization measurements for Mn_xTiS_2 ($x = 0.01, 0.05$, and $1/3$) at 4.2 K. It is found that the σ - H curves for $x \leq$

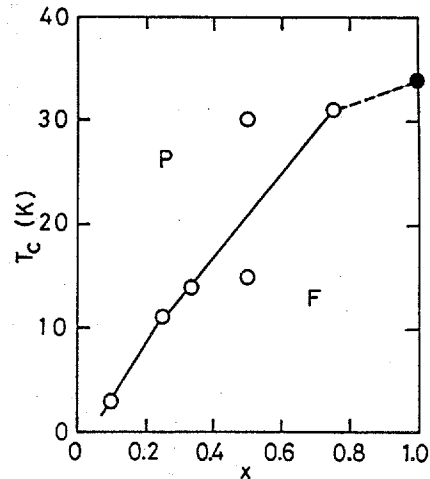


Fig. 8. Magnetic phase diagram of Cr_xTiS_2 .

0.01 are linear and those for $0.10 \leq x \leq 1/3$ are near-linear, while those for intermediate Mn concentration $0.03 \leq x \leq 0.10$ are non-linear (S-letter like curve) but with no hysteresis. Even though the overall σ -H curves of Mn_xTiS_2 are paramagnetic, there are different interactions involved. Considering these experimental data, together with the ESR studies²⁴⁾ which show that an exchange narrowing for $x \leq 0.10$ and a dipolar broadening for $x > 0.10$ are found in the linewidths, we may expect that in the low concentration regions $x \leq 0.10$ some ferromagnetic exchange interactions exist, showing that the Mn 3d electrons are rather localized, while in the higher regions $x > 0.10$ the guest 3d electrons are spread into a band.

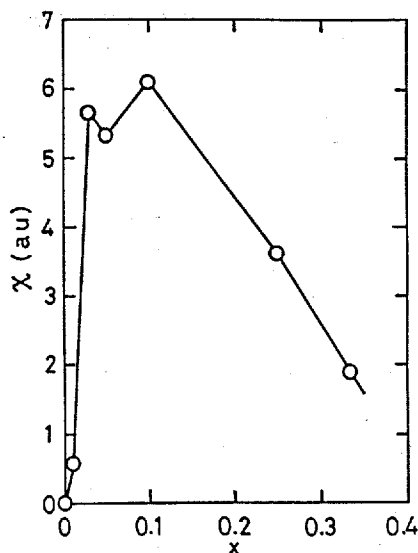


Fig. 10. Intensities of the ac susceptibilities at 4.2 K plotted against x for Mn_xTiS_2 .

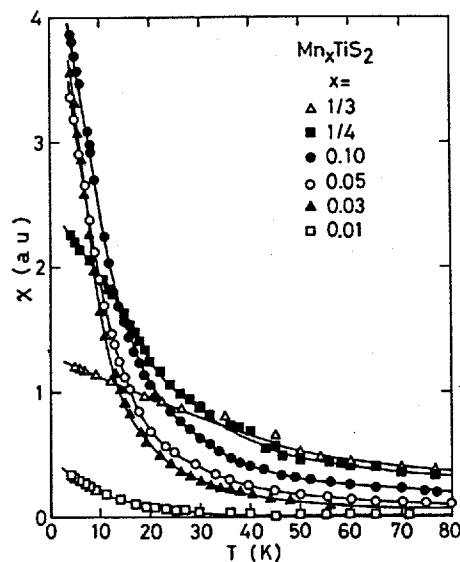


Fig. 9. Temperature dependence of the ac magnetic susceptibility of Mn_xTiS_2 .

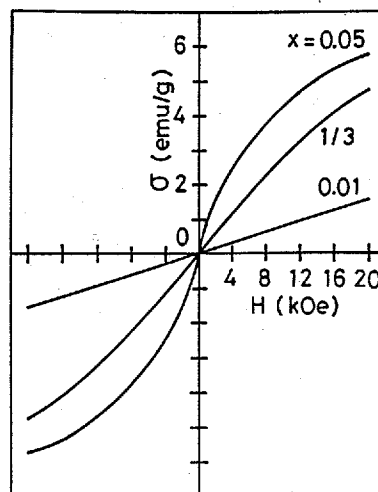


Fig. 11. Magnetization curves at 4.2 K for Mn_xTiS_2 .

3.2.4. Fe_xTiS_2

Figure 12 illustrates the ac susceptibilities χ for Fe_xTiS_2 ($0.01 \leq x \leq 1$) over the temperature 1.5-300 K; the inset shows the χ -T curves for $x = 0.01-0.20$. The relative intensities of χ increase roughly with Fe concentration x . For a very low concentration $x = 0.01$, the ac susceptibility follows simply a paramagnetic Curie-Weiss behavior. Those for $0.05 \leq x \leq 0.20$ show a cusp at the charac-

teristic temperature. For $x \geq 1/4$ (except $x = 1/2$), a marked peak at the characteristic temperature T_C is observed. The temperature dependences of ac susceptibilities in static fields for $\text{Fe}_{0.20}\text{TiS}_2$ and $\text{Fe}_{1/2}\text{TiS}_2$ are shown in Fig. 13(a) and (b), respectively. In the case of $\text{Fe}_{0.20}\text{TiS}_2$ (and other samples with $x \leq 0.40$), as the dc field is increased the position of the cusp appears to shift progressively to a lower temperature side;

similar field dependences are observed for a number of spin-glass systems, which is attributed to a random distribution of magnetic clusters of different size and anisotropy fields²⁵⁾ or negative nonlinear susceptibility χ_2 .^{26,27)} On the contrary, for $\text{Fe}_{1/2}\text{TiS}_2$ (and other samples with $x > 0.40$) the peak temperature shifts to a higher temperature side with increasing the dc field. The increase in the apparent ferromagnetic Curie temperature is due to the superposition of an internal field and externally applied field, as found in usual ferromagnets.

Figure 14 shows the results of the pulsed field magnetization curves at 4.2 K

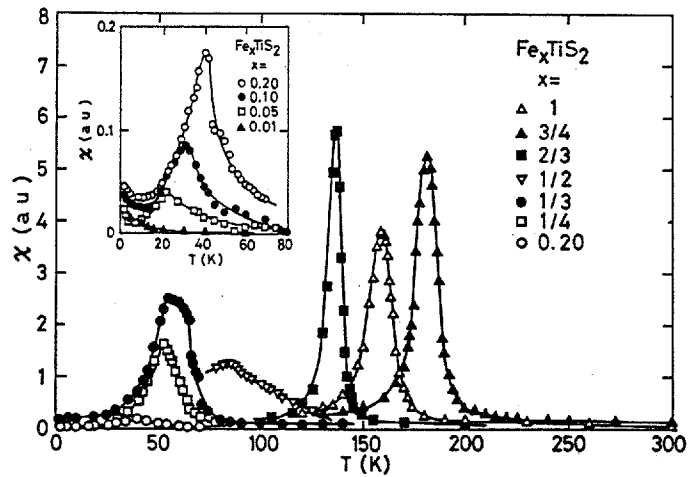


Fig. 12. Temperature dependence of the ac magnetic susceptibility of Fe_xTiS_2 ; inset shows the enlarged χ - T curves for $x = 0.01$ - 0.20 .

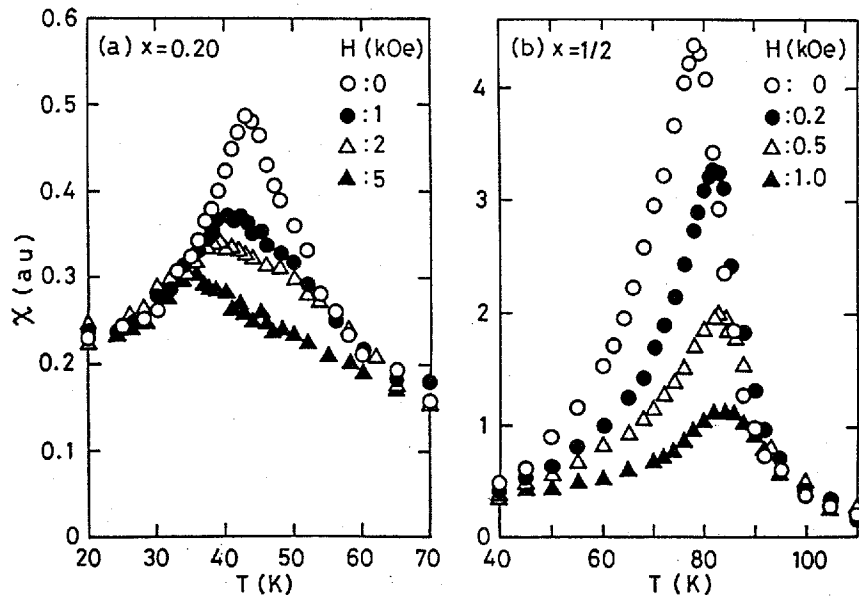


Fig. 13. Temperature dependence of the ac magnetic susceptibilities χ in static fields H for (a) $\text{Fe}_{0.20}\text{TiS}_2$ and (b) $\text{Fe}_{1/2}\text{TiS}_2$.

for Fe_xTiS_2 with different Fe concentration. Each magnetization curve shows a hysteresis with a large coercive force H_C (11–41 kOe) and a remanent magnetization σ_r (4–40 emu/g) that depend on x . For low concentrations ($x = 0.20$ and $1/3$) the initial magnetizations increase gradually with increasing field, whereas for high concentrations ($x = 2/3$ and $3/4$) they increase sharply at fields corresponding to the coercive forces. In particular, $\text{Fe}_{3/4}\text{TiS}_2$ shows a two-step rise in the magnetization σ , which means that the domain wall motion proceeds with two steps. Furthermore, we should note that such a large hysteresis curve in the high field σ - H curve is observed even for $x = 0.20$, whose temperature dependence of the

low-field ac susceptibility shows a cusp around 43 K characteristic of a spin-glass state. The coercive forces H_C of Fe_xTiS_2 at 4.2 K are plotted against x in Fig. 15. With increasing x H_C attains a maximum at $x = 0.15$ and a minimum at $x = 0.40$, and then increases sharply up to $x = 0.60$, followed by a decrease. We note that the increase in H_C for $x > 0.40$ corresponds to the increase in the Curie temperature T_C (see Fig. 16). We have also confirmed that the coercive forces of the as-grown crystals for $x \geq 1/2$ (average size: 0.1 mm) are smaller than those of the powdered samples (average size: 0.10 mm). Such a size dependence of H_C for $x \leq 0.40$ is slightly small. Eibschutz et al.¹⁰⁾ have found similarly a large coercive force ($H_C \sim 55$ kOe) in $\text{Fe}_{0.28}\text{TiS}_2$ and the single domain size of the order of 100–150 Å. As pointed out by them, the observed magnetization curves for $x > 0.40$ are due to an

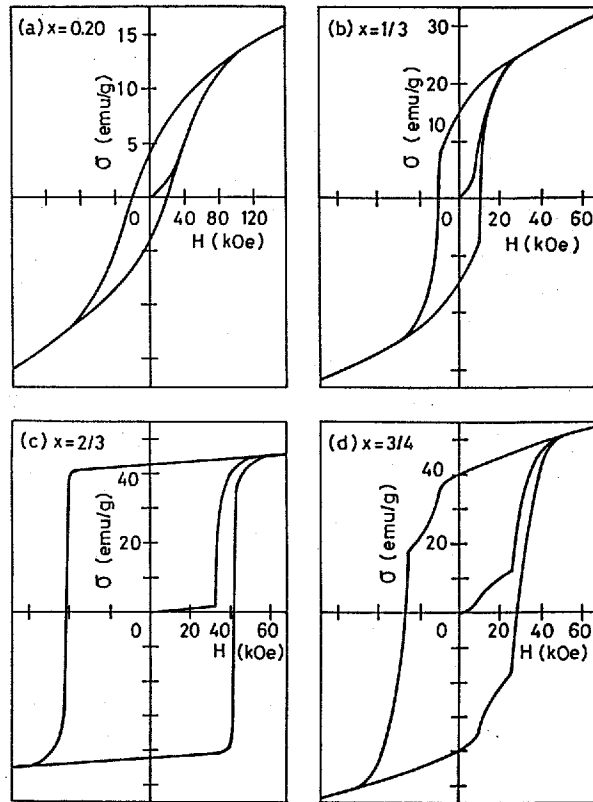


Fig. 14. Magnetization curves at 4.2 K for Fe_xTiS_2 .

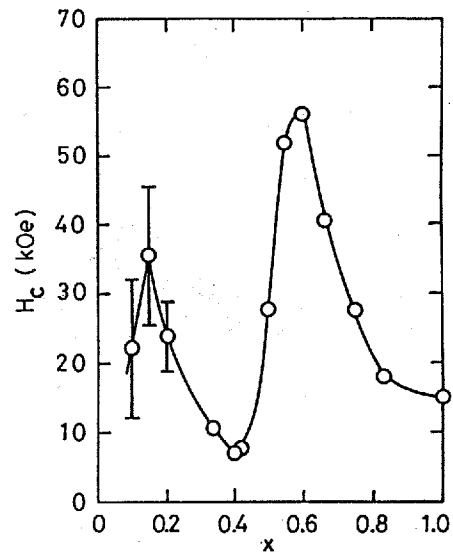


Fig. 15. Coercive force H_C at 4.2 K plotted against x for Fe_xTiS_2 .

incoherent rotation of magnetic spins.

From the foregoing experimental results, we obtain the phase diagram of Fe_xTiS_2 as shown in Fig. 16, which consists of three magnetic ordered phases. In the low Fe concentration $x \leq 0.20$ a spin-glass (SG) phase appears, in the intermediate range $0.20 < x \leq 0.40$ there is something like a cluster-glass (CG) or micromagnetic phase, and in the high region $x > 0.40$ a ferromagnetic phase dominates. In addition to the σ -H and χ -T data, we have also measured the specific heats C ,²⁷⁾ according to which the anomalies in the C -T curves for $x \geq 1/2$ are observed at the Curie temperatures, while no anomalies are detected for the samples showing the SG and CG phases. This phase diagram is in agreement with that reported by Yoshioka et al.,¹⁵⁾ who observed no spontaneous magnetization for $x < 0.38$. Moreover, the concentration dependence of the transition temperature T_C suggests an itinerant magnetic character, which is supported by the photoemission studies¹⁷⁾ and the calculation of the energy bands of M_xTiS_2 .^{18,19)}

Furthermore, we have measured the anisotropy in the ac susceptibility of single crystalline samples. A typical result for $\text{Fe}_{1/4}\text{TiS}_2$ is shown in Fig. 17. When the ac field h is applied parallel to the c -axis, χ shows a peak around $T_C =$

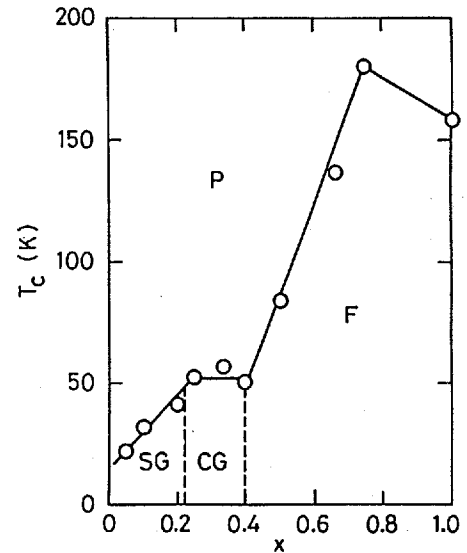


Fig. 16. Magnetic phase diagram of Fe_xTiS_2 ; spin-glass (SG), cluster-glass (CG), and ferromagnetism (F).

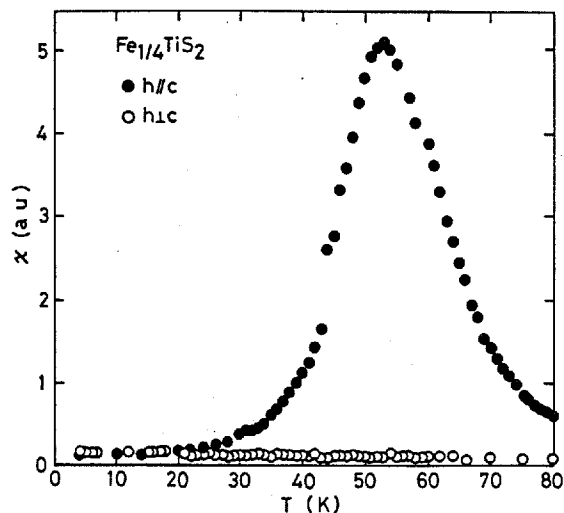


Fig. 17. Anisotropy in the ac magnetic susceptibility of $\text{Fe}_{1/4}\text{TiS}_2$.

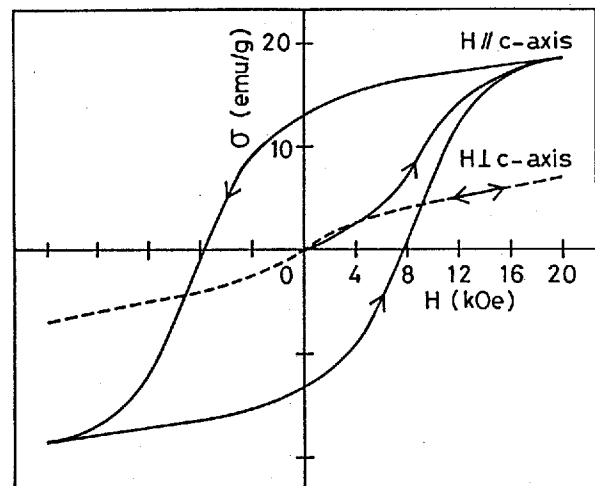


Fig. 18. Anisotropy in the magnetization curve at 4.2 K for $\text{Fe}_{1/3}\text{TiS}_2$.

52 K, whereas it is temperature independent when h is perpendicular to the c -axis, indicating that the Fe spins align preferentially along the c -axis. In Fig. 18 is shown a typical result for anisotropy in the σ - H curve of $\text{Fe}_{1/3}\text{TiS}_2$ at 4.2 K. In the magnetic field parallel to the c -axis the σ - H curve shows a hysteresis with a coercive force of 7.7 kOe, whereas in the field parallel to the c -axis the σ - H curve is nearly linear. This result reveals that the magnetic easy-axis in Fe_xTiS_2 is parallel to the c -axis, in agreement with the ac susceptibility. Such a strong anisotropy in Fe_xTiS_2 may be due to the anisotropic Fermi surface; this picture is in contrast with those for $\text{Fe}_{1/3}\text{NbS}_2$,^{11,12)} $\text{Fe}_{0.28}\text{TaS}_2$ ¹⁰⁾ and $\text{Fe}_{1/3}\text{TaS}_2$,¹²⁾ where the anisotropy can be understood in terms of a crystalline field model of the splitting of the d levels on the Fe^{2+} ($3d^6$) ions, as discussed by Parkin and Friend.¹²⁾

To supplement the above magnetic data, we also measured the Mössbauer effect for Fe_xTiS_2 . In Fig. 19 are shown the typical results of ^{57}Fe Mössbauer spectra for $x = 0.10$, $1/3$, and 1 at 300 K. Fe_xTiS_2 shows a single peak with the isomer shift $\delta = 0.78$ mm/s and a small shoulder with $\delta \sim 0$ may be due to the presence of a small superparamagnetic impurity of α -Fe fine particle. The Fe intercalates with $x = 0.10$ and $1/3$ show a small quadrupole splitting 2ϵ with the isomer shift 0.75 - 0.76 mm/s. The asymmetry of the observed spectra is due to a preferred orientation of the flakes used. The values of isomer shift are 0.7 - 0.8 mm/s for all compounds, which corresponds to the value for FeS where the iron atoms are surrounded octahedrally by S atoms and the Fe-S bond is rather covalent. This indicates that the Fe atom occupies the octahedral site in the van der Waals gap and becomes the divalent ion Fe^{2+} (d^6) in a high spin state with some covalent Fe-S bonding, as pointed out in the structural studies.

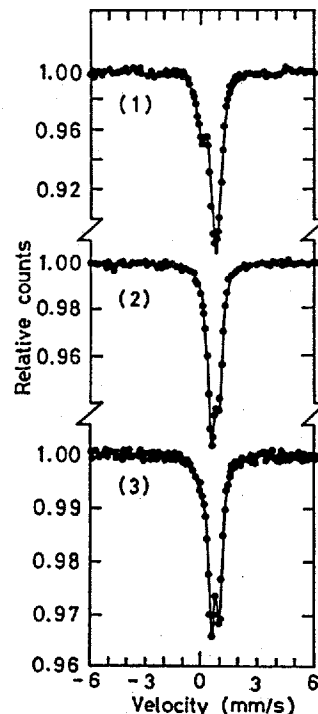


Fig. 19. Typical Mössbauer spectra at 300 K for Fe_xTiS_2 with (1) $x = 1$, (2) $1/3$, and (3) 0.10 .

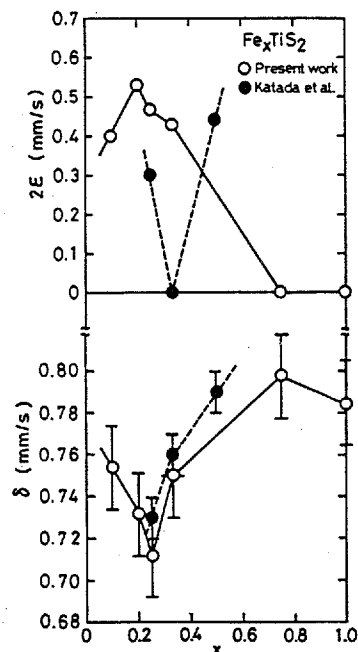


Fig. 20. Isomer shift δ and quadrupole splitting 2ϵ at 300 K plotted against x for Fe_xTiS_2 ; the results by Katada et al.²⁹⁾ are shown by solid circles.

Table III. The lattice constants a and c , axial ratio c/a , isomer shift δ , and quadrupole splitting 2ε for Fe_xTiS_2 at 300 K

x	a (Å)	c (Å)	c/a	δ (mm/s)	2ε (mm/s)
0.10	3.412	5.722	1.677	0.75	0.40
0.20	3.413	5.706	1.672	0.73	0.53
1/4	3.416	5.708	1.671	0.71	0.47
1/3	3.420	5.716	1.671	0.75	0.43
3/4	3.427	5.798	1.692	0.80	0.00
1	3.428	5.809	1.695	0.78	0.00

Our result is in good agreement with those for $x = 1/4$, $1/3$, and $1/2$ by Katada et al.²⁹⁾ The concentration dependences of the isomer shift δ and the quadrupole splitting 2ε are illustrated in Fig. 20, together with the results by Katada et al.²⁹⁾ The value of δ attains a minimum at $x = 1/4$ and a maximum at $x = 3/4$. Since in general δ is large when the chemical bond between the ion and a ligand is ionic, the above results show the change in the ionicity of the Fe-S bond with Fe concentration. The quadrupole splitting 2ε attains a maximum at $x = 0.20$ and vanishes for $x \geq 3/4$. This behavior corresponds qualitatively to the change in the axial ratio c/a , as listed in Table III. Thus it appears that the quadrupole hyperfine interaction reflects the anisotropic trigonal field around the Fe ions. The concentration dependence of δ by Katada et al. agree with our results but not for 2ε . Moreover, we note that there is a good relationship between δ and 2ε , though not shown here. At any rate, it should be emphasized that in view of the ^{57}Fe Mössbauer data alone a localized picture seems to be valid in Fe_xTiS_2 , which apparently contradicts to the itinerant magnetic picture as mentioned previously. This is because the Mössbauer spectroscopy sees only a local field of the Fe nuclei, compared with the overall Fe 3d stated by other methods.

3.2.5. Co_xTiS_2

The experimental results for Co_xTiS_2 ($0.075 \leq x \leq 1/2$) are shown in Fig. 21. For low Co concentrations $x \leq 0.05$ and high concentrations $x \geq 1/2$, the ac susceptibilities obey a paramagnetic Curie-Weiss law. In the intermediate concentration range ($0.075 \leq x \leq 1/3$), the ac susceptibilities rise steeply

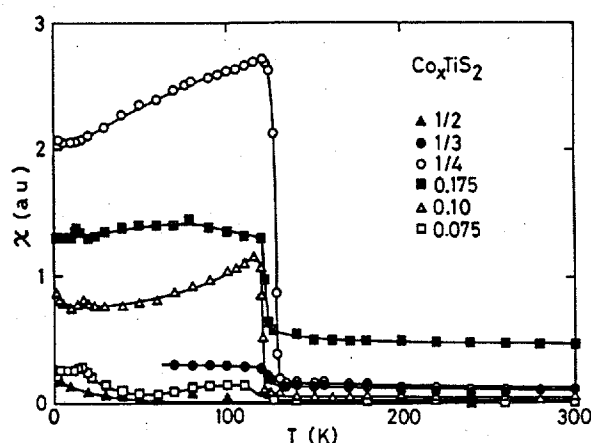


Fig. 21. Temperature dependence of the ac magnetic susceptibility for Co_xTiS_2 .

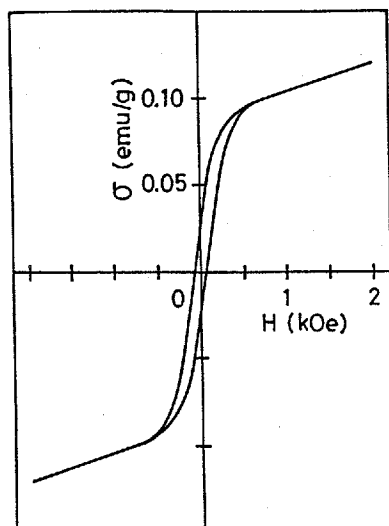


Fig. 22. Magnetization curves at 77 K for $\text{Co}_{1/4}\text{TiS}_2$.

at a characteristic temperature T_c as the temperature is lowered, showing the existence of a magnetic ordered phase. In contrast to Fe_xTiS_2 , the χ - T curves of Co_xTiS_2 below T_c are nearly constant, indicating that this compound is rather a "soft" magnetic material. Furthermore, the additional phase transitions observed at low temperatures for $x = 0.075, 0.10$ and 0.175 may be due to other changes in physical parameters such as coercive force etc.

The magnetization measurements for Co_xTiS_2 show that only magnetic ordered phase appears within a restricted range of the Co concentration $0.075 \leq x \leq 1/3$. As an example, Fig. 22 depicts the σ - H curve for $\text{Co}_{1/4}\text{TiS}_2$ at 77 K in the magnetic field up to 2 kOe, which shows a hysteresis with a small coercive force of 60 Oe, indicating a soft ferromagnet. The magnetization σ does not saturate but continues to increase linearly with H . The absolute value of σ is very small compared with those of Fe_xTiS_2 ; e.g., $\sigma = 0.25$ emu/g or $5.7 \times 10^{-3} \mu_B/\text{Co}$ for $\text{Co}_{1/4}\text{TiS}_2$ at 10 kOe. In Fig. 23 are plotted against x the values of σ_0 obtained by extrapolating the high field σ - H curves to zero field, and the high field susceptibilities χ_H or paramagnetic susceptibilities χ_p at 77 K. The magnetization σ_0 is non-zero only in

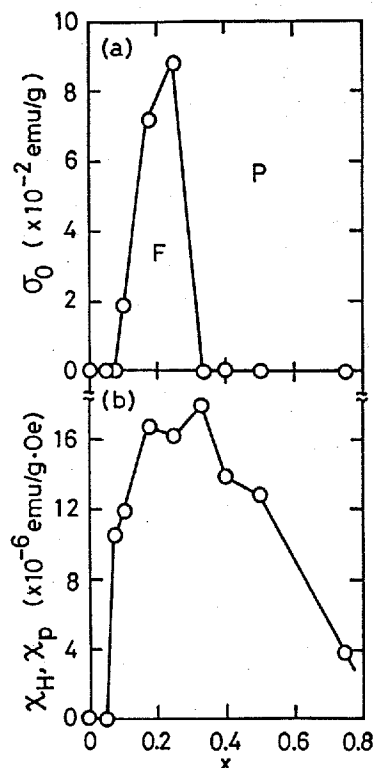


Fig. 23. (a) The magnetization σ_0 obtained by extrapolating the σ - H curves to zero field and (b) high field susceptibilities χ_H (the slopes of the σ - H curves at high field) or paramagnetic susceptibilities χ_p at 77 K plotted against x for Co_xTiS_2 .

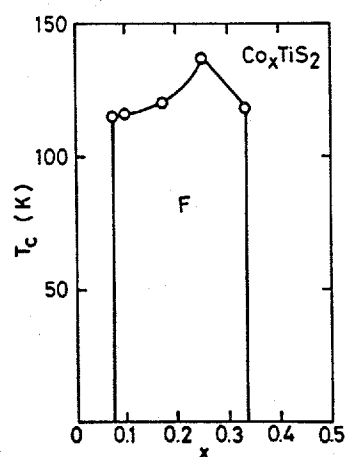


Fig. 24. Magnetic phase diagram for Co_xTiS_2 .

the restricted concentration range $x = 0.10$ – $1/4$, corresponding to the phase diagram. The values of χ_H or χ_p increase with x up to $x = 0.20$, remain nearly constant in the range $0.20 \leq x \leq 1/3$, followed by a gradual decrease. In the paramagnetic phase ($x \geq 0.40$), if a localized model is valid, χ_p should be proportional to the amount of the intercalated Co atoms, in contrast to the experimental results. The observed decrease in χ_p with x can be understood by an itinerant or band picture. As is well known, a spin paramagnetic susceptibility χ_s is written by $\chi_s = 2D(E_F)/(1 - \xi)$, where $D(E_F)$ is the density of states at the Fermi energy E_F and $1/(1 - \xi)$ the Stoner enhancement factor. Since $D(E_F)$ of Co_xTiS_2 with $x > 1/4$ is approximately independent of x ,²⁸⁾ the observed decrease in χ_p is attributable to the decrease in ξ with increasing x . The magnetic transition temperature T_c as a function of x for Co_xTiS_2 thus obtained is shown in Fig. 24. It is characteristic of this system that the magnetic orderings appear only in the restricted range of Co concentration ($0.075 \leq x \leq 1/3$).

3.2.6. Ni_xTiS_2

Figure 25 shows the results for Ni_xTiS_2 ($0.05 \leq x \leq 3/4$). For low Ni concentrations $x \leq 0.40$ the ac susceptibilities obey a paramagnetic Curie-Weiss law, while for high concentrations $x \geq 1/2$ Ni_xTiS_2 shows marked peaks at the characteristic temperature

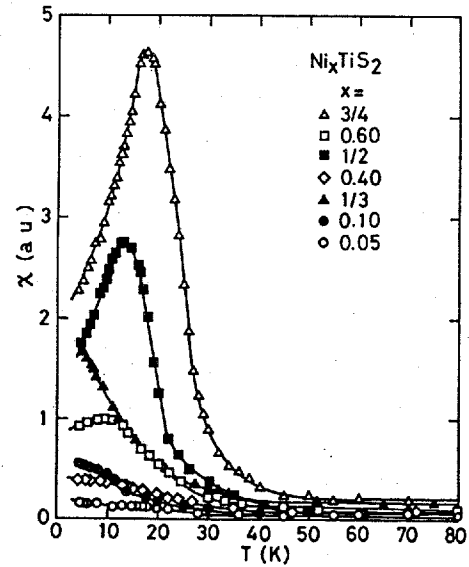


Fig. 25. Temperature dependence of the ac magnetic susceptibility of Ni_xTiS_2 .

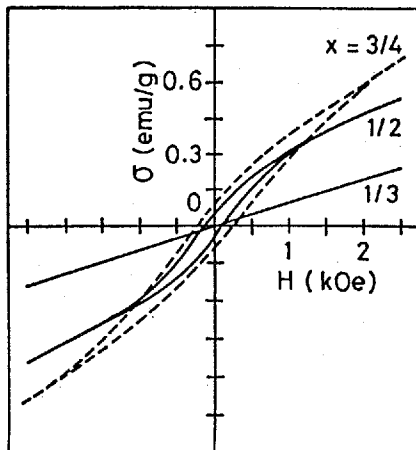


Fig. 26. Magnetization curves at 4.2 K for Ni_xTiS_2 .

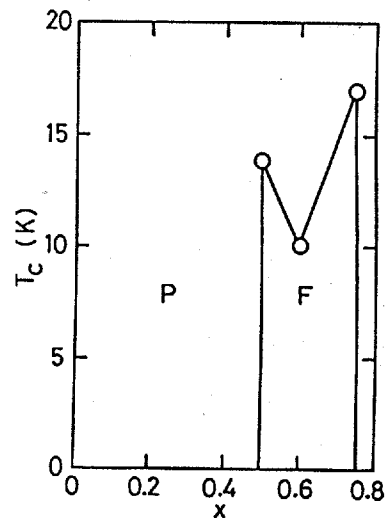


Fig. 27. Magnetic phase diagram of Ni_xTiS_2 .

T_C (10-20 K), showing some magnetic ordered state. The magnetic ordered phase of Ni_xTiS_2 , which appears solely in the range $1/2 \leq x \leq 3/4$ according to the ac susceptibility data, has now been confirmed to be ferromagnetic, as shown in Fig. 26, where the σ - H curves at 4.2 K for $x = 1/3, 1/2$, and $3/4$ are illustrated. The Curie temperature T_C is of the order of 10-17 K and the coercive force of the order of 200 Oe in Ni_xTiS_2 . The phase diagram of Ni_xTiS_2 is shown in Fig. 27.

3.2.7. $M_{1/3}TiS_2$

To see the difference among the guest 3d metals, we show in Fig. 28 the pulsed field magnetization curves up to 160 kOe at 4.2 K for $M_{1/3}TiS_2$; at this particular guest concentration $x = 1/3$, the $\sqrt{3}a \times \sqrt{3}a$ superstructure is formed. Only the Fe intercalate shows a large hysteresis curve. In Fig. 29 are plotted the values of σ or μ in units of μ_B/atom at 160 kOe against the atomic number of the guest 3d metals. The overall behavior resembles the well-known Slater-Pauling curve, except for Co atom, which also supports that an itinerant or band picture rather than a localized model is appropriate for understanding the magnetic properties of M_xTiS_2 . The small value of μ for Co atom has been attributed to the low-spin state ($d\epsilon$)⁶ ($d\gamma$)¹ of Co^{2+} ion, as found in ESR²⁴) and structural studies.

Table IV lists the types of magnetism for $M_{1/3}TiS_2$, together with those for $M_{1/3}NbS_2$ and $M_{1/3}TaS_2$, as well as the easy axis of magnetization predicted by Parkin et al.¹²) for comparison. $Cr_{1/3}TiS_2$ is ferromagnetic, $Fe_{1/3}TiS_2$ is a CG state, $Co_{1/3}TiS_2$ is weak-ferromagnetic, and others are paramagnetic. Only the Fe

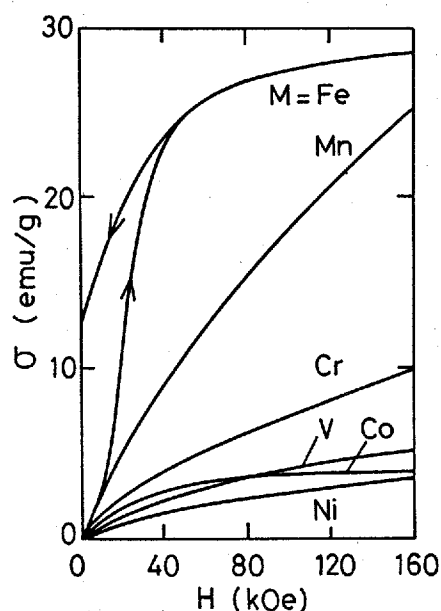


Fig. 28. High field magnetization curves at 4.2 K for $M_{1/3}TiS_2$ ($M = V, Cr, Mn, Fe, Co$, and Ni).

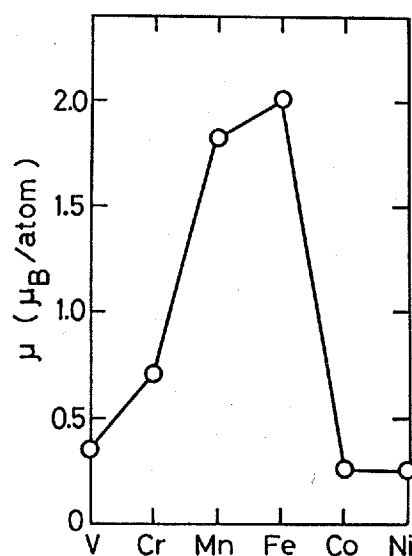


Fig. 29. The values of σ or μ in units of μ_B/atom at 160 kOe and 4.2 K plotted against the atomic number of the guest 3d metals.

Table IV. Type of magnetism in $\text{M}_{1/3}\text{TiS}_2$, $\text{M}_{1/3}\text{NbS}_2$, and $\text{M}_{1/3}\text{TaS}_2$; P, F, WF, AF, and CG stand for para-, ferro-, weak-ferro-, antiferromagnetism, and cluster-glass, respectively. The symbols // and \perp denote the easy axis of magnetization parallel and perpendicular to the c-axis, respectively

M	V	Cr	Mn	Fe	Co	Ni
$\text{M}_{1/3}\text{TiS}_2$ ^{a)}	P	F	P	CG//	WF	P
$\text{M}_{1/3}\text{NbS}_2$	F \perp ^{b)}	F \perp ^{b)}	F \perp ^{c)}	AF// ^{c)}	AF ^{c)}	AF ^{c)}
$\text{M}_{1/3}\text{TaS}_2$ ^{b)}	F \perp	F \perp	F \perp	F //	AF	AF
Easy axis ^{b)}	\perp	\perp		//	\perp	\perp

^aPresent work, ^bParkin et al.¹²⁾, ^cFriend et al.¹¹⁾

intercalate shows a strong anisotropy with the easy axis parallel to the c-axis. The magnetic anisotropy in $\text{Fe}_{1/3}\text{NbS}_2$ and $\text{Fe}_{1/3}\text{TaS}_2$ has been ascribed to a strong crystal field around the intercalated Fe^{2+} ion and to a strong spin-orbit coupling, all of which are based on a rigid or localized model.¹²⁾ In our case, where a band picture is valid, the anisotropy may be due to an anisotropic shape of the Fermi surface.

4. Summary

3d transition metal intercalation compounds M_xTiS_2 have been grown by the chemical vapor transport technique. The X-ray analysis shows that the interlayer spacing a remains unchanged with x, while the interlayer spacing c is strongly dependent on the metals and x. By electron diffraction observations of Mn, Fe, Co, and Ni intercalates, the superstructures at $x = 1/4$ and $1/3$ have been confirmed. Based on the concept of "resonance" in chemical bonding introduced by Pauling, we have attempted to explain semiempirically the variation of interlayer spacing c with intercalation of 3d transition metals into 1T-CdI_2 type TiS_2 layers, by taking into account the ionic radii, bond lengths, force constants, and bond ionicity. We have shown that overall agreement between the model calculation and experiments is excellent. However, the bonding nature is actually not so simple but complicated. Our proposed model must further be refined by considering the changes in the intralayer spacing a and the interatomic distance d_1 between the Ti and S atoms, which we have assumed constant, or the interactions between next-nearest atomic bonds.

Furthermore, the exhaustive magnetic studies on M_xTiS_2 have been carried through, such as low-field ac magnetic susceptibility measurements in the temperature range 1.5–300 K and magnetization measurements at 4.2, 77, 300 K using a vibrating sample magnetometer up to 20 kOe and a pulse magnet up to 160 kOe. Also ^{57}Fe Mössbauer spectra at 300 K and the ac magnetic susceptibilities in static fields up to 5 kOe have been measured on Fe_xTiS_2 . The characteristic features are

summarized below.

- i) V_xTiS_2 is a paramagnetic material over the whole composition of x .
- ii) Mn_xTiS_2 ($x \leq 1/3$) is also paramagnetic, but in the low concentration range $x \leq 0.10$ the intercalated Mn 3d electrons are regarded as localized and some ferromagnetic exchange interactions exist, while in the higher region $x > 0.10$ the 3d electrons form a band.
- iii) A ferromagnetic ordered phase is found in Cr_xTiS_2 with $x \leq 3/4$; $CrTiS_2$ ($x = 1$) shows an antiferromagnetic behavior.
- iv) The magnetic phase diagram of Fe_xTiS_2 falls into three regions; a spin-glass phase for $x \leq 0.20$, a cluster-glass or mictomagnetic phase for $0.20 < x \leq 0.40$, and a hard ferromagnetic phase for $x > 0.40$. Over the whole concentration range the high field magnetization curves exhibit a hysteresis with a large coercive force H_c (7-56 kOe) and a strong anisotropy. The concentration dependences of isomer shift δ and quadrupole splitting 2ϵ have been found. From the order of magnitudes of δ we may conclude that the Fe atom occupies the octahedral site of the van der Waals gap in the form of divalent Fe^{2+} (d^6) with high-spin state, accompanying a covalent Fe-S bonding.
- v) Co_xTiS_2 shows weak-ferromagnetism in the restricted range of $0.075 \leq x \leq 1/3$.
- vi) A ferromagnetic ordered state is found in Ni_xTiS_2 for $1/2 \leq x \leq 3/4$.
- vii) The magnetic moment at 4.2 K and 160 kOe versus the atomic number of guest 3d metals for $M_{1/3}TiS_2$ resembles the Slater-Pauling curve.

All these experimental results, together with the resonant photoemission data,¹⁷⁾ support that an itinerant or band picture is valid rather than a localized or rigid band model in these intercalation compounds, in agreement with the recent band calculations using a self-consistent APW method.^{18,19)}

Acknowledgments

The author would like to express his sincere thanks to Professor M. Inoue for valuable advice and continuing encouragement in the course of the present work. He is also grateful to Professor emeritus T. Yasunaga for heartfelt encouragement, Professor Y. Komura for the use of X-ray apparatus and Professor H. Fujiwara for useful advices. Also he thanks Dr. A. Kumao of Kyoto University of Industrial Arts and Textile Fibers for carrying out the electron diffraction observations and Dr. H. Sakai of Research Reactor Institute of Kyoto University for Mössbauer spectroscopy measurements on our samples at their laboratories and for valuable suggestions. Thanks are due to Professor K. Motizuki of Osaka University and Dr. H. Kadomatsu for valuable discussions and suggestions. Furthermore, he is indebted to colleagues and students in Inoue Laboratory for useful discussions and their help in taking the experimental data. At last, he thanks Mrs. R. Tsukamoto and M. Fujimoto for their encouragements.

References

- 1) J. A. Wilson and A. D. Yoffe, *Adv. Phys.*, **18**, 193 (1969).
- 2) M. S. Whittingham, *Prog. Solid State Chem.*, **12**, 41 (1978).
- 3) J. M. Vandenberg-Voorhoeve, "Structural and Magnetic Properties of Layered Chalcogenides of the Transition Elements", in "Optical and Electrical Properties", ed by P. A. Lee, D. Reidel, Dordrecht (1976), pp. 423-458.
- 4) G. V. Subba Rao and M. W. Shafer, "Intercalation in Layered Transition Metal Dichalcogenides", in "Intercalated Layered Materials", ed by F. Levy, D. Reidel, Dordrecht (1979), pp. 99-200.
- 5) A.R. Beal, "The First Transition Metal Complexes of Some Group VA Transition Metal Dichalcogenides", in "Intercalated Layered Materials", ed by F. Levy, D. Reidel, Dordrecht (1979), pp. 251-306.
- 6) M. S. Whittingham, *J. Electrochem. Soc.*, **123**, 315 (1976).
- 7) L. Trichet, J. Rouxel, and M. M. Pouchard, *J. Solid State Chem.*, **14**, 283 (1975).
- 8) T. Miyadai, K. Kikuchi, H. Kondo, S. Sakka, M. Arai, and Y. Ishikawa, *J. Phys. Soc. Japan*, **52**, 1394 (1983).
- 9) F. Hulliger and E. Pobitschka, *J. Solid State Chem.*, **1**, 117 (1970).
- 10) M. Eibshutz, F. J. DiSalvo, G. W. Hull and S. Mahajan, *Appl. Phys. Lett.*, **27**, 464 (1975).
- 11) R. H. Friend, A. R. Beal, and A. Yoffe, *Phil. Mag.*, **35**, 1269 (1977).
- 12) S. S. P. Parkin and R. H. Friend, *Phil. Mag.*, **41**, 65 (1980).
- 13) Y. Tazuke and T. Endo, *J. Magn. Magn. Mat.*, **31-34**, 1175 (1983).
- 14) M. Danot, J. Rouxell, and O. Gorochoy, *Mat. Res. Bull.*, **9**, 1383 (1974).
- 15) T. Yoshioka and Y. Tazuke, *J. Phys. Soc. Japan*, **54**, 2088 (1985).
- 16) S. Muranaka, *Mat. Res. Bull.*, **8**, 679 (1973).
- 17) Y. Ueda, H. Negishi, M. Koyano, M. Inoue, K. Soda, H. Sakamoto, and S. Suga, *Solid State Commun.*, **57**, 839 (1986).
- 18) T. Yamasaki, N. Suzuki, and K. Motizuki, *J. Phys.*, **C20**, 395 (1987).
- 19) N. Suzuki, T. Yamasaki, and K. Motizuki, *Int. Symp. on Intermetallic Compounds, Apr. 20-22, 1987, Kyoto, Japan, J. Magn. Magn. Mat.* (1987) (in press).
- 20) L. Pauling, "The Nature of the Chemical Bond", Cornell University Press, Ithaca (1960), 3rd ed.
- 21) M. Inoue, M. Matsumoto, H. Kadomatsu and H. Fujiwara, *J. Phys. Soc. Japan*, **53**, 48 (1984).
- 22) L. Rouxel, A. Le Blanc, and A. Royer, *Bull. Soc. Chim. Fr.*, **6**, 2019 (1971).
- 23) R. D. Shannon and C. T. Prewitt, *Acta Crystallogr., Sect. B*, **25**, 925 (1969).
- 24) M. Inoue and H. Negishi, *J. Phys. Soc. Japan*, **54**, 380 (1985).
- 25) A. K. Grover, S. K. Malik, C. Radhakrishnamurty, and R. Vijayaraghavan, *Solid State Commun.*, **32**, 1323 (1979).
- 26) S. Chikazawa, D. J. Sandberg, and Y. Miyako, *J. Phys. Soc. Japan*, **50**, 2884 (1981).
- 27) M. Suzuki, *Prog. Theor. Phys.*, **58**, 1151 (1977).
- 28) M. Inoue, Y. Muneta, H. Negishi, and M. Sasaki, *J. Low Temp. Phys.*, **63**, 235 (1986).
- 29) M. Katada and R. H. Herber, *J. Solid State Chem.*, **33**, 361 (1980).